Supplementary Information for

Raman interrogation of the ferroelectric phase transition in polar metal LiOsO$_3$

Feng Jin[a, b], Le Wang[a], Anmin Zhang[e], Jianting Ji[a], Youguo Shi[a], Xiaoqun Wang[c], Rong Yu[b, □], *Jiandi Zhang[d, □], E.W. Plummer[d, □]*, and Qingming Zhang[a, e, □]

[a]*Beijing National Laboratory for Condensed Matter Physics, Institute of Physics, Chinese Academy of Sciences, Beijing 100190, China*
[b]*Department of Physics, Renmin University of China, Beijing 100872, China*
[c]*Department of Physics and Astronomy, Shanghai Jiao Tong University, Shanghai 200240, China*
[d]*Department of Physics and Astronomy, Louisiana State University, Baton Rouge, LA 70803, USA*
[e]*School of Physical Science and Technology, Lanzhou University, Lanzhou 730000, China*

□ To whom correspondence should be addressed. Email: qmzhang@ruc.edu.cn, wplummer@phys.lsu.edu, mailto:jiandiz@lsu.edu, or rong.yu@ruc.edu.cn

This PDF file includes:

S1. Additional results of *T*-dependence of phonon modes

Figure S1 shows *T*-evolution of the P1, P2 and P3 modes. With increasing temperature, the intensity of P1, P2 and P3 modes decrease gradually, disappearing for $T > T_s$, thus confirm that these three modes exist only in the low-*T* ferroelectric phases. For example, the P1, P2 and P3 modes disappear in the spectra collected at 140 and 145 K (see Fig. S1B). It should be noted that the broad and small hump (below P3 mode) are irrelevant to the phase transition discussed here since it located at the same position with no change for all measured temperatures (Fig. S1C). A zoom plot of the P2 mode can be found in the inset of Fig. S1B, which clearly show that the mode disappears when $T > T_s$. The intensities shown in Fig. 1C have been normalized with respect to the intensities at 10 K and by a Bose-Einstein factor.

Based on the above observation (gradually decreasing of the intensity of P1, P2 and P3 modes and the non-observation of these modes for $T > T_s$), along with the behavior of order parameter extracted from the intensity of these modes, we conclude that the ferroelectric phase transition is a second-order order-disorder transition.
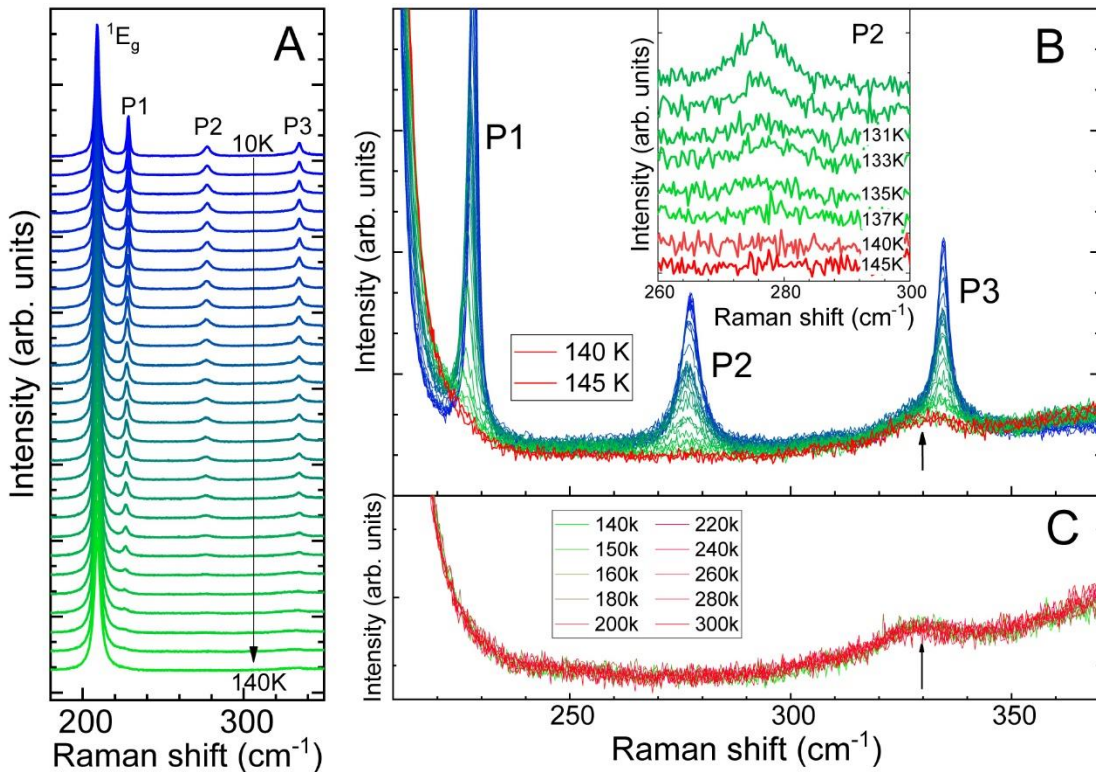

Figure S1. *T*-dependence of Raman spectra for P_1, P_2 and P_3 modes displayed (**A**) with and (**B**) without an equal amount of vertical shift for each spectrum. The inset is the *T*-dependence of P2-mode near the phase transition temperature T_s ~137K. (**C**) The Raman spectra above T_s in the energy range where P_1, P_2 and P_3 modes appear. There is a *T*-independent mode marked by arrow.

Figure S2 provides the detailed evolution of the three E_g modes with temperature

across the ferroelectric phase transition. Although both ^2E_g and ^3E_g are the modes involved with the vibration of Li, it is ^3E_g mode which is associated with the vibration of Li like the A_u mode (Fig. 1 in the main text) and couples with the A_u mode. Thus, ^3E_g is the best candidate to monitor the ferroelectric phase transition due the polar instability related to the A_u mode. Figure S2A displays the Raman spectra as a function of temperature, from $T = 10$ to 300 K for an energy range covering all phonon modes (three P and three E_g modes). P1, P2 and P3 appears only below T_s when the system is in ferroelectric phase, while three E_g modes appear in both paraelectric and ferroelectric phase. The evolution of measured phonon energy and linewidth for three E_g modes are displayed in Fig. S2B-G. Anomalies of these quantities near T_s are evident with the largest changes for the ^3E_g mode. It should be noted that these figures are obtained by fitting the spectra with Fano line shape, where the detail fitting procedure can be found in section S2.

In order to provide the frequency shift intrinsically due to the ferroelectric phase transition, the ordinary T-dependent phonon frequency $\omega_0(T)$ without any phase transition has to be subtracted from measured data. Considering the contributions due to the thermal

effects, $\omega_0(T)$ can be expressed as $\omega_0(\mathrm{T}) = \omega_0 - C\left(1 + \dfrac{2}{e^{\frac{\hbar\omega_0}{2k_BT}}-1}\right)$ and obtained by

fitting the measured frequency data $\omega_{ph}(T)$ for $T > 180$ K to the expressed function, where ω_0 is the extrapolated frequency at $T = 0$ K. The fitting results of $\omega_0(T)$ for these three E_g modes are shown as dashed curves in Fig. S2B-2D as compared with the measured $\omega_{ph}(T)$ (blue circles). The frequency shift intrinsically due to the phase transition, $\Delta\omega \equiv \omega_{ph}(T)$-$\omega_0(T)$, can be obtained and the results of the relative Raman shift ($\Delta\omega/\omega_0(T_s)$) for the three E_g modes are presented in Fig. 1E in the main text. The T-evolution of phonon linewidth (red circles) for these modes are shown in the same scale and the thermal

contribution (dashed lines) are modeled with function $\Gamma_0(\mathrm{T}) = \Gamma_0\left(1 + \dfrac{2}{e^{\frac{\hbar\omega}{2k_BT}}-1}\right)$, where

Γ_0 is the linewidth at 10 K (precisely, it should be at T = 0K). Compared with the linewidth of ^1E_g and ^2E_g modes, the linewidth of ^3E_g mode exhibits the largest changes with a diverge feature near T_s. The above quantitative analysis of these three E_g modes (frequency and linewidth) suggest that the ^3E_g mode, which is dominated by the Li vibration, is unique.
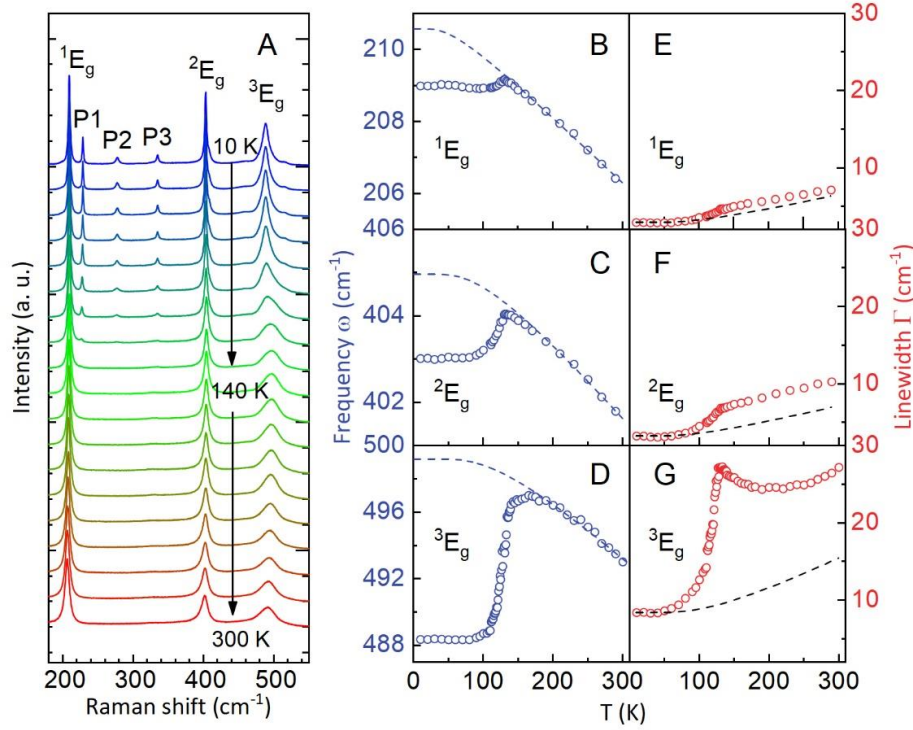
Figure S2. Overview of observed E_g modes and the uniqueness of the ^3E_g modes. (A) T-dependent Raman spectra of the observed E_g modes. (B-G): T-dependence of the frequency and linewidth of (B) ^1E_g, (C) ^2E_g, and (D) ^3E_g mode, respectively. The ordinary T-dependent phonon frequency $\omega_0(T)$ (linewidth $\Gamma_0(T)$) are depicted by the dashed blue (black) curves.

S2. Details of the fitting procedure

To quantify the observed changes of the ^3E_g mode, we have fitted the temperature evolution of the spectrum with Fano function ($I_\omega = \frac{I_0(q+\varepsilon)^2}{1+\varepsilon^2}$) plus a linear background ($I_{back} = A\omega + C$), where $\varepsilon = (\omega - \omega_0)/\Gamma$ with ω_0 is the bare phonon frequency and Γ is the linewidth. q is the asymmetry parameter and $|1/q|$ is the asymmetry factor. To subtract a reliable background, we used the high-energy spectrum section between 560 and 590 cm^{-1} (far away from any peak) for the background fitting. The obtained slope (A) of the linear background monotonically changes with temperature from almost zero at 10 K to ~ -0.4 at 300 K.

In Figure S3, we show the Raman spectra and the corresponding fitted line shapes at several selected temperature, 10 K, 90 K, 140 K and 300 K, from which one can see that the Fano function gives a good description of the line shape of ^3E_g mode.
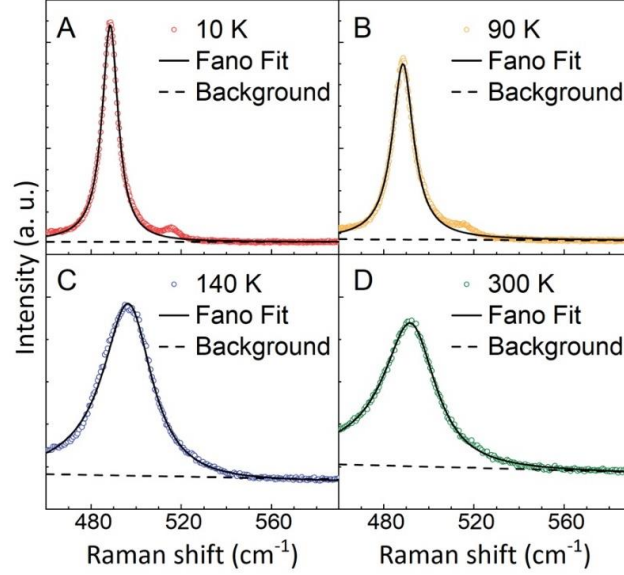
Figure S3. Raman spectra and the corresponding Fano-fitted line shape (solid black lines) of the ^3E_g mode at 10 K, 90 K, 140 K and 300 K. The dashed lines represent the fitted linear background. And the fitting parameters are shown in the table below.

Temperature T (K)	Frequency ω_0 (cm^{-1})	Linewidth Γ (cm^{-1})	Asymmetry factor $|1/q|$	Slope of background
10	488.3	8.4	0.006	0.0153
90	488.4	11.1	0.005	-0.0811
140	496.5	26.2	0.06	-0.1961
300	493.0	27.2	0.07	-0.3782

Table 1: Fitting parameters for the ^3E_g spectra at 10 K, 90 K, 140 K and 300 K.

S3. Pseudospin-phonon interaction

According to the pseudospin-phonon interaction model developed by Schaack and Winterfeldt [1], the Hamiltonian $H_{\sigma-ph}$ is given by

$$H_{\sigma-ph} = H_L + H_S + H_{L,S}$$

where H_L is the harmonic lattice Hamiltonian, H_S is the pseudospin Hamiltonian and $H_{L,S}$ is the term describing the interaction between phonons and pseudospins, which can be expressed as

$$H_{L,S} = \sum_k U(k)\,Q(k)S(k) + \sum_{k,k'} U(k,k')Q(k)Q^*(k,k')S(k') + \cdots$$

Here, $Q(k)$ represents the normal coordinate of a given normal mode with the wave vector k, $U(k)$ a coupling constant and $S(k)$ the Fourier transform of the z projection of the pseudospin operator.

In order to account for the frequency shifts, we need to include the terms that are at

least quadratic in the normal mode coordinates. In such a case, the renormalization of the phonon frequencies for $k' = 0$ can be expressed as

$$\omega_{ph}^2 = \omega_0^2 + 2U(k)\langle S(0)\rangle,$$

where ω_0 is the phonon frequency without coupling to pseudospin and $U(k)$ represents a coupling constant. By assuming that the mean value of $S(0)$ is proportional to the order parameter, i.e., $P_s \propto \langle S(0)\rangle$, we obtain the Eq. (1) given in the main text.

On the other hand, in this model, the critical broadening of the linewidth of phonon is due to the energy fluctuations of the phonon modes and can be expressed as

$$\Gamma_{sp}^2 = \langle\left(\omega_{ph} - \langle\omega_{ph}\rangle\right)^2\rangle \propto \langle S^2(0)\rangle - \langle S(0)\rangle^2 \propto \langle P^2\rangle - \langle P\rangle^2 = \frac{kT\chi(0)}{V}$$

where V is the volume of the crystal, $\chi(0)$ is the dielectric susceptibility and $\langle P\rangle$, $\langle P\rangle^2$ represents the mean and mean square of the polarization, respectively. The above equation is exactly Eq. (2) in the main text.

S4. Magnetoresistance measurements

To further investigate the electronic scattering and the message of the Fermi surface, we performed magnetoresistance (MR) measurements for the present sample at representative temperatures (Fig. S4A). One can see that the MRs increase monotonically with decreasing temperature, where the magnetoresistance $\text{MR} = \frac{\rho(H)-\rho(0)}{\rho(0)}$, $\rho(H)$ and $\rho(0)$ represents the transverse magnetoresistance at a magnetic field H and that at zero field at a given temperature, respectively. Although the MRs are very weak, i.e., less than 3% at 14 T and 2 K, they exhibit a well H^2 dependence for the whole field range. The semiclassical transport theory [2] has predicted that if only one isotropic relaxation time is present in a solid-state system, Kohler's rule will hold. it can be written as

$$\text{MR} = \frac{\rho(H) - \rho(0)}{\rho(0)} = \frac{\Delta\rho}{\rho(0)} = F(H\tau) \qquad (5)$$

where, τ represents the relaxation rate. If the factor $m^*/{ne^2}$ does not change with temperature, equation (5) can be simplified (since $\rho(0) = m^*/{ne^2\tau}$)

$$\text{MR} = \frac{\rho(H) - \rho(0)}{\rho(0)} = \frac{\Delta\rho}{\rho(0)} = F\left(\frac{H}{\rho(0)}\right) \qquad (6)$$

Then the magnetoresistance $\text{MR} \propto \frac{H^2}{\rho^2(0)}$ because of the H^2 dependence of the MRs in the present system (see Fig. S4A). Therefore, a plot of MR versus $\frac{H^2}{\rho^2(0)}$ (Kohler's plot)

is expected to collapse into a single *T*-independent curve if the Kohler's rule is obeyed. Figure S4B presents the Kohler's plot of our data at several representative temperatures. Clearly, the MR data measured at different temperatures do not collapse into a single *T*-independent curve, and thus, the Kohler's rule is not obeyed in $LiOsO_3$.

We now consider four possible explanations for the violation of Kohler's rule in $LiOsO_3$, within the framework of semi-classical transport theory.

(i) *The electronic structure varies with temperature due to the structure transition*. This can explain the violation of the Kohler's rule and the strong temperature dependence of the R_H. However, to the best of our knowledge, almost all calculations find little changes of the band structure between the two phases [3, 4, 5]. What's more, if the violation of Kohler's rule is due to the change of electronic structure, the Kohler's rule should hold when the temperature is far below T_s because of the stability of electronic structure at the low temperatures. However, this is inconsistent with our observations.

(ii) *There is more than one type of carrier and their mobility have different temperature dependences (multiband effect)*. To illustrate how this can lead to the violation of the Kohler's rule we consider the case of two band model [2]. In this model, MR can be expressed as follows by omitting the higher-order term of $\mu_0 H$

$$\Delta\rho/\rho(0) \simeq \frac{\sigma_1\sigma_2(\mu_1 - \mu_2)^2 B^2}{(\sigma_1+\sigma_2)^2}$$

where $\sigma_i = n_i e^2 \tau/m_i$ and $\mu_i = e\tau/m_i$ are the conductivity and the mobility of the ith-band, respectively, with n_i and m_i are the charge-carrier density and the effective mass of the ith-band, respectively. The negative value and linear field dependence of ρ_{xy} (Fig. 3A) indicates that all carriers should be electron type and the small magnetoresistance (Fig. S4A) at the whole temperatures suggest that these electrons should have similar mobility. Thus, the multiband effect is also unlikely the cause of the violation of Kohler's rule.

(iii) *The density of charge carrier varies with temperature*. For this case, equation (6) will not be held, and then a plot of MR versus $\frac{H^2}{\rho^2(0)}$ will not collapse into a single curve.

However, equation (5) is still to hold, and through which we get that $1/\tau \propto MR^{-\frac{1}{2}} \propto T^{2.4}$, as shown in the Fig. S4C. And then we get that the density of carrier *n* changes as $T^{-1.1}$, since $\rho(0) = \frac{m^*}{ne^2\tau}$ and $\rho \propto T^{3.5}$ (Fig. S4D). The resultant $T^{1.1}$-dependence of the density of carrier means that the absolute value of R_H will increases with increasing temperature, which is inconsistent with our observations.
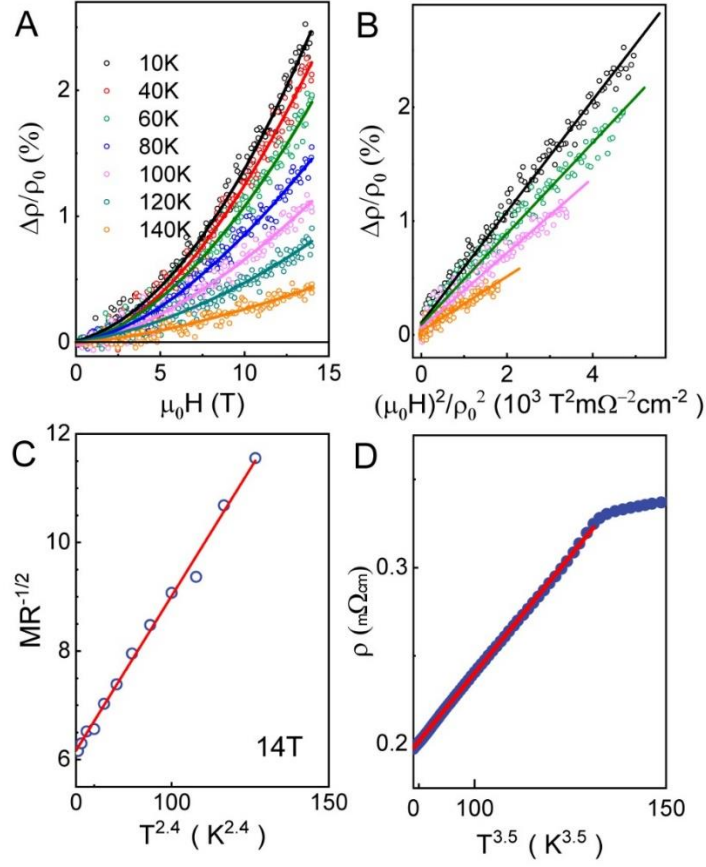
Figure S4. Anisotropic electron scattering rate evidenced by magnetoresistance measurements. (**A**) Field-dependence of magnetoresistance $\frac{\Delta\rho}{\rho(0)}$. The solid lines are a H^2 fit to the measured data at corresponding temperatures. (**B**) Kohler's plot [see Eq. (6)] of the magnetoresistance. (**C**) $T^{2.4}$-dependence of the MR$^{-1/2}$ at 14 T. The magnetoresistance (MR) at 14 T was obtained through the fitting lines in (A). (**D**) $T^{3.5}$-dependence of the electrical resistivity ρ for $T < T_s$. The lines in (B) and (C) are a linear fit to the corresponding data and the line in (D) is a $T^{3.5}$ fit to the electrical resistivity.

(iv) *The T-dependence of scattering rate varies significantly at different points over the Fermi surface*. In this case, the only one isotropic relaxation time assume of Kohler's rule will not be held and leading to the violation of the Kohler's rule. The strong *T*-dependence of anisotropic scattering can also give rise to a strong temperature dependence of Hall coefficient R_H, since it is given by [2]

$$R_H = \frac{1}{ne}\frac{\langle\tau^2\rangle}{\langle\tau\rangle^2}$$

where $\langle...\rangle$ denotes an average over the Fermi surface. This explanation is consistent with our observations.

Figure S4 displays the T-dependence of the magnetoresistance $\frac{\Delta\rho}{\rho(0)}$ and the graphic evidence of the violation of Kohler's rule. As shown in Fig. S4A, LiOsO₃ has a rather small magnetoresistance (< 3%) even at very low temperature. Figure S4B presents a plot of $\frac{\Delta\rho}{\rho(0)}$ versus $\frac{H^2}{\rho^2(0)}$. The data at different temperatures do not collapse into a single line, indicating the violation of Kohler's rule. By analyzing the T-dependent magnetoresistance and electrical resistivity data, we conclude that the scattering rate of electron over the Fermi surface are anisotropic.

S5. Details of the theoretical model

In this section, we discuss some details of the pseudospin-fermion model we proposed. The Hamiltonian is given in Eq. 4 of the main text. To construct this model, we first note that in the ferroelectric phase compared to the Li ion displacement, the shifts of Os and O ion positions are negligible [4, 5]. We thus assume zero displacement of Os and O ions in the ferroelectric phase and describe the Li ion displacement by an Ising pseudospin variable σ^z, since a Li ion could take either of two possible positions. The long-range Coulomb repulsion between two Li⁺ ions generates an effective ferroelectric coupling between two pseudospins ($J_{ij} > 0$ in Eq. 4 of the main text).

As another simplification we adopted, we assume that besides the positively charged Li⁺ ions, all charges are distributed around the Os positions (so that the Os ions are effectively negatively charged). This can be achieved theoretically by symmetrizing the electron wave functions on O ions. With these assumptions, we can construct a tight-binding model for the electrons located on Os ions that are responsible for the metallicity of the system. The model generally includes both Os $5d$ and O $2p$ orbitals, and the tight-binding parameters can be obtained by fitting to DFT band structure [4, 5].

The Coulomb interaction between the Li⁺ ions and electrons in the system gives rise to couplings between the pseudospins and itinerant electrons. To a first-order approximation, the Li⁺ displacement acts a static electric field proportional to σ^z on the itinerant electrons. Such an electric field leads to a Stark effect to the electrons, which mixes electron wavefunctions in orbitals with different parities. This effect, in particular the hybridization between the Os $5d$ and O $2p$ orbitals, has been taken into account by the second term of Hamiltonian in Eq. 4 of the main text. Because of the broken inversion symmetry by the ferroelectric distortion, the hybridization gives rise to a noncentrosymmetric distribution of the electron wave functions, as shown in Fig. 4A of the main text. The electron density then has a spatially inhomogeneous distribution, with higher electron density closer to the displaced Li⁺ ions (see Fig. 4B of the main text). In this way, the ferroelectric polarization generated by the Li⁺ distortion is partially screened by the itinerant electrons.

To see how the itinerant electrons interplay with the local electric dipoles σ^z, we first define a hybridized basis of the itinerant electrons

$$c_{i\pm} = \frac{1}{\sqrt{2}}\left(c_{id} \pm c_{ip}\right)$$

The Hamiltonian in Eq. 4 of the main text is then rewritten to

$$H = \sum_{\langle ij\rangle\alpha\beta} t_{ij}^{\alpha\beta}\, c_{i\alpha}^{\dagger}c_{j\beta} - \frac{K}{2}\sum_{i}\left(c_{i+}^{\dagger}c_{i+} - c_{i-}^{\dagger}c_{i-}\right)\left(\sigma_{i+\delta}^{z} + \sigma_{i-\delta}^{z}\right) - \sum_{\langle ij\rangle}J_{ij}\,\sigma_{i+\delta}^{z}\sigma_{j+\delta}^{z}$$
$$+ H_{\sigma-ph}$$

Here we can define a orbital pseudospin operator $\sigma_{ci}^{z} = c_{i+}^{\dagger}c_{i+} - c_{i-}^{\dagger}c_{i-}$. The itinerant electrons interact with the local electric dipoles via a dipole-dipole interaction $\sigma_{ci}^{z}\sigma_{i\pm\delta}^{z}$. $H_{\sigma-ph}$ refers to the pseudospin-phonon coupling that accounts for the phonon anomaly at T_s discussed in the main text. Its explicit expression can be found in Sec. S3 or Ref. [1]. It is irrelevant to the interaction between itinerant electrons and pseudospins and is hence dropped in the following discussion. We can then integrate out the itinerant electrons from the Hamiltonian, and obtain an effective Hamiltonian for the local electric dipoles $\sigma_{i\pm\delta}^{z}$:

$$H_{eff} = -\sum_{\langle ij\rangle}(J_{ij} + J_{ij}^{c})\sigma_{i+\delta}^{z}\sigma_{j+\delta}^{z}$$

where $J_{ij}^{c} \sim \left[2k_F r_{ij}\cos\left(2k_F r_{ij}\right) - \sin\left(2k_F r_{ij}\right)\right]/r_{ij}^{4}$ is the effective dipole-dipole interaction mediated by itinerant electrons. It has a form similar to the RKKY interaction [6], and depending on the inter-dipole distance, it can be either ferro-electric ($J_{ij}^{c}> 0$) or

anti-ferroelectric ($J_{ij}^{c}< 0$). In particular, for small Fermi momentum k_F, $J_{ij}^{c}< 0$ up to a

certain number of neighbor pairs. The anti-ferroelectric couplings will strongly renormalize the direct interactions between the local electric dipoles, and even introduce frustrated interactions. Such an effect accounts for the suppression of the ordered moment in the ferroelectric phase. In the meantime, the excitation of itinerant electrons produces an imaginary part to the dynamical dielectric susceptibility $\chi(q, \omega)$, that introduces a damping term to the local electric moments. Such a damping effect is similar to the one in the Hertz-Millis theory of spin density waves [7, 8], and is also known to suppress the ordered moment. As a result of the suppression of the ordered moment, the ordering process in $LiOsO_3$ is much slower than that in the insulating ferroelectric compounds, as shown in Fig. 1D of the main text. In addition, the damping also suppresses the value of

the dielectric susceptibility. Note that in the paraelectric phase, $\chi = \dfrac{1}{T-\theta}$, where

$\theta \sim J_{eff} \sim J_{ij} + J_{ij}^c$. Curie-Weiss temperature θ is thus reduced by the coupling between local electric dipoles and itinerant electrons. On the other hand, the structural transition takes place when further couple the local dipoles to symmetry-related lattice distortions (due to the $H_{\sigma-ph}$ term), which makes T_s slightly larger than J_{eff}. As a result, the fitted Curie-Weiss temperature θ is smaller than T_s (see Fig. 2H of the main text).

The ferroelectric ordering also influences the transport properties of the itinerant electrons. As shown in Fig. 4D of the main text, the ferroelectric ordering turns on a channel of electron hopping via the Os-Li-Os path. This is a second-order effect, and modifies the electron dispersion by $(-\Delta t_a^2 \eta^2 / \epsilon_{Li})sin^2(k_z/2)$, where Δt_a is the change of hopping matrix associated with the ferroelectric ordering, and ϵ_{Li} refers to the onsite energy of the Li^+ ion. Note that such a term only modifies the dispersion of itinerant electrons along the k_z direction and serves as an additional source of electronic anisotropy in the ferroelectric phase. In addition, the relaxation time associated with the Os-Li-Os scattering also changes, as the effect of Li^+ disorder is diminished by the ferroelectric ordering. The additional electronic anisotropy in the ferroelectric phase is reflected in the change of slope of the measured Hall coefficient in Fig. 3 of the main text.

References:

1. Schaack G, Winterfeldt V (1977) Temperature behavior of optical phonons near T_c in triglycine sulphate and triglycine selenate. *Ferroelectrics* 15:35-41.
2. Hurd CM (1972) *The Hall Effect in Metals and Alloys* (Springer, New York).
3. Sim H, Kim BG (2014) First-principles study of octahedral tilting and ferroelectric-like transition in metallic $LiOsO_3$. *Phys Rev B* 89:201107.
4. Liu HM, et al. (2015) Metallic ferroelectricity induced by anisotropic unscreened Coulomb interaction in $LiOsO_3$. *Phys Rev B* 91:064104.
5. Giovannetti G, Capone M (2014) Dual nature of the ferroelectric and metallic state in $LiOsO_3$. *Phys Rev B* 90:195113.
6. Kasuya TA (1956) Theory of metallic ferro- and antiferromagnetism on Zener's model. *Prog Theor Phys* 16:45.
7. Hertz JA (1976) Quantum critical phenomena. *Phys Rev B* 14:1165.
8. Millis AJ (1993) Effect of a nonzero temperature on quantum critical points in itinerant fermion systems. *Phys Rev B* 48:7183.